EES Catalysis

PAPER

View Article Online
View Journal | View Issue

Cite this: *EES Catal.*, 2023, 1, 695

Hydrogen spillover in Pt_5Ru_1 nanoalloy decorated Ni_3S_2 enabling pH-universal electrocatalytic hydrogen evolution†

Zuxi Yu,[a] Xianhong Rui [b] and Yan Yu *[ac]

Received 30th January 2023,
Accepted 18th May 2023

DOI: 10.1039/d3ey00020f

rsc.li/eescatalysis

As a new type of clean energy, hydrogen receives extensive attention due to its zero-pollution characteristics. Hydrogen produced by electrocatalysis is extensively studied due to its convenient properties. However, most catalysts for catalyzing the hydrogen evolution reaction are noble metals, which hinders their commercialization. Herein, we design a very effective electrocatalyst of Ni_3S_2 decorated with a small amount of Pt_5Ru_1 nanoalloy supported on Ni foam (Ni_3S_2/Pt_5Ru_1@NF) to enhance its hydrogen evolution reaction kinetics by exploiting the hydrogen spillover effect between Pt_5Ru_1 and Ni_3S_2. The designed Ni_3S_2/Pt_5Ru_1@NF exhibits excellent HER performance under both acidic and alkaline conditions, achieving a current density of 10 mA cm^{-2} at only 13 mV and 42 mV, respectively.

Broader context

As a clean energy source with zero pollution, hydrogen has been paid more and more attention. Electrocatalytic hydrogen production is an effective and rapid synthetic method. Most electrocatalytic hydrogen production relies on noble metal catalysts, which increases the cost of hydrogen synthesis. At present, many non-noble metal catalysts have been reported for the hydrogen evolution reaction, but most of them have poor performance. In this work, we designed a Ni_3S_2 catalyst, which was decorated with a small amount of Pt_5Ru_1 nanoalloy. This structure can effectively reduce the hydrogen evolution barrier by the hydrogen spillover effect. As a highly efficient hydrogen evolution catalyst, the designed Pt_5Ru_1 nanoalloy decorated Ni_3S_2 (Ni_3S_2/Pt_5Ru_1@NF) can significantly reduce the hydrogen evolution overpotential. This work could provide theoretical guidance and experimental evidence for designing high catalytic activity and high stability hydrogen evolution electrocatalysts and give fundamental insight into the potential construction of advanced electrocatalysts. We are sure that our work is very valuable to the readers of this journal and will attract a lot of attention.

1. Introduction

As the world continues to transition toward carbon emission-free energy technologies, it is necessary for us to reduce the carbon emissions of the chemical production industry.[1] Hydrogen, featured by high gravimetric energy density and zero-emission, holds great potential as a sustainable alternative to fossil fuels.[2] Electrocatalytic water splitting is an efficient method for producing high-purity hydrogen, but this method is far from cost-competitive with commercial steam reforming for hydrogen production.[3] At present, people are devoted to finding electrocatalysts with high catalytic performance and long life in extreme acid–base environments.[4,5] In general, catalyst design for electrocatalytic hydrogen evolution reactions is guided by the classical volcano theory, in which the free energy of hydrogen adsorption on the catalyst surface is an important indicator.[6] The theory points out that the adsorption energy for protons is neither too strong nor too weak, which should favor the protons gaining electrons at the active sites and easily leaving the surface to form hydrogen gas.[7] The elements at the top of the volcano map have thus been a hot research topic. Platinum, a representative of the precious metals, has become the target of choice for the commercial electrocatalytic production of hydrogen.[8] However, its high price and weak hydrogen evolution performance under alkaline conditions hinder its further application.[9] Therefore, the development of electrocatalysts with no noble metal or low noble metal content is the focus of current research.

Various terrestrially abundant and inexpensive transition metal compounds have been explored, among which sulfides have

[a] *Hefei National Research Center for Physical Sciences at the Microscale, Department of Materials Science and Engineering, CAS Key Laboratory of Materials for Energy Conversion, University of Science and Technology of China, Hefei, Anhui 230026, China. E-mail: yanyumse@ustc.edu.cn*
[b] *School of Materials and Energy, Guangdong University of Technology, Guangzhou, 510006, China*
[c] *National Synchrotron Radiation Laboratory, Hefei, Anhui 230026, China*

† Electronic supplementary information (ESI) available. See DOI: https://doi.org/10.1039/d3ey00020f

been extensively studied due to their novel physicochemical properties.[10] There are numerous reports on the role of sulfides in electrocatalytic hydrogen evolution, among which the Ni_3S_2 catalyst stands out due to its unique electronic structure.[11–15] However, recent studies have shown that the inherent activity of Ni_3S_2 is insufficient, and its intrinsic catalytic activity is at least two orders of magnitude worse than that of noble metals,[16] which may be related to the unfavorable free energy of hydrogen adsorption on the surface of Ni_3S_2. Many methods have been utilized to modify the Ni_3S_2 catalyst, including doping, introduction of vacancy defects, and interfacial engineering, but simply modifying the electronic and geometric structures of the Ni_3S_2 catalyst cannot effectively compensate for its intrinsically poor activity. Inspired by the phenomenon of hydrogen spillover induced by strong metal–support interactions during thermal hydrogenation, hydrogen spillover has recently emerged as a research frontier in HER electrocatalysts.[17,18] This strategy utilizes the difference in the free energy of hydrogen adsorption between metals and supports to kinetically facilitate the adsorption and desorption of protons.[19,20] The binary 'metal–support' system with the hydrogen spillover effect has great potential to boost the performance of the Ni_3S_2 catalyst with less metal usage.

Herein, we designed a binary 'metal–support' electrocatalyst based on Ni_3S_2 decorated with Pt and Ru nanoalloys on Ni foam (NF). By introducing a small amount of noble metal elements, the hydrogen evolution performance of Ni_3S_2@NF in acidic and alkaline solution can be greatly improved. Meanwhile, compared with Pt nanoparticles, the work function difference ($\Delta\phi$) between the Pt_5Ru_1 nanoalloy and Ni_3S_2 substrate is smaller, which effectively prevents charge accumulation at the interface and enhances the hydrogen overflow process. The unique structure of Ni_3S_2/Pt_5Ru_1@NF provides a new idea for designing high catalytic activity and high stability hydrogen evolution electrocatalysts.

2. Results and discussion

Microstructure characterization

The Ni_3S_2/Pt_5Ru_1@NF catalyst was prepared by a one-step hydrothermal method, followed by a chemical reduction reaction. Specifically, Ni_3S_2 was synthesized *in situ* on a nickel foam substrate by a hydrothermal method, and then H_2PtCl_6 and $RuCl_3$ were reduced at room temperature to obtain the Ni_3S_2/Pt_5Ru_1@NF heterostructure catalyst. The detailed process is illustrated in the Experimental section. X-ray diffraction (XRD) characterization was employed to identify the crystal structure of the as-prepared Ni_3S_2/Pt_5Ru_1@NF sample. As presented in Fig. 1a, two dominant peaks appearing at 2θ of 44.5° and 51.8° are assigned to the pristine Ni foam substrate (PDF#04-0850).[21] Additionally, other diffraction peaks are well matched with hexagonal heazlewoodite Ni_3S_2 (PDF#44-1418).[22] Due to the small size and low loading of the catalyst, no XRD peaks for the supported metal are clearly observed. The weight ratio of supported metal catalysts of Pt to Ru was determined to be 5 : 1 by inductively-coupled plasma mass spectrometry (ICP-MS, Table S1, ESI†). Scanning electron microscopy (SEM) and transmission electron microscopy (TEM) were carried out to investigate the morphology and microstructure of Ni_3S_2/Pt_5Ru_1@NF. The SEM images (Fig. S1, ESI†) show that Ni_3S_2 is densely loaded on the surface of nickel foam, and Pt_5Ru_1 nanoalloys are grown on Ni_3S_2. In contrast, the surface of the Ni foam is smoother (shown in Fig. S2a, ESI†) and the surface graininess was increased after loading Ni_3S_2, as shown in Fig. S2b (ESI†). The TEM image (Fig. 1b) also shows that nanoparticles with an average size of 5 nm are uniformly decorated on the supported submicron particles. The corresponding FFT patterns (insets in Fig. 1b) reveal that the particles really are Pt_5Ru_1 ($Fm\bar{3}m$), and Ni_3S_2 (R32). The interplanar spacings of 0.287 and 0.225 nm correspond to the (110) facet of Ni_3S_2 and (111) facet of Pt, respectively. Owing to the close interplanar spacing between Ru and Pt, Ru atoms can fill in the Pt lattice to form nanoalloys in a ratio of 5 : 1, which is proved by line scanning (Fig. S3, ESI†). Additionally, the STEM image (Fig. 1c) and its corresponding elemental mappings prove that Pt_5Ru_1 nanoalloys are evenly distributed on the surface of the Ni_3S_2 substrate. The chemical compositions and valence states of Ni_3S_2/Pt_5Ru_1@NF were examined by X-ray photoelectron spectroscopy (XPS). As shown in Fig. 1d–g, the XPS spectra of Ni_3S_2/Pt_5Ru_1@NF testify the presence of elemental Ni, S, Pt and Ru, which is consistent with the EDX results. As for the high-resolution Ni 2p spectrum of Ni_3S_2/Pt_5Ru_1@NF in Fig. 1d, two visible peaks located at binding energies of 873.6 and 855.7 eV are assigned to the Ni $2p_{1/2}$ and Ni $2p_{3/2}$ orbital of Ni^{2+}, respectively.[23,24] Compared with Ni_3S_2@NF (Fig. S4, ESI†), the peaks of Ni in Ni_3S_2/Pt_5Ru_1@NF shift to higher energy, indicating that there is interfacial electron transfer between the Pt_5Ru_1 nanoalloy and Ni_3S_2, and more electrons flow to the Pt_5Ru_1 nanoalloy.[25] No obvious change has been observed in the peaks of S (Fig. 1e), indicating that the electron transfer mainly occurs between the metal elements. Compared with Pt foil, the Pt in Ni_3S_2/Pt_5Ru_1@NF shows a 0.5 eV negative shift in Fig. 1f.[15] And a slight negative shift of Ru in Ni_3S_2/Pt_5Ru_1@NF is also observed in Fig. 1g compared to Ru foil. The electron transfer process between Pt_5Ru_1 nanoalloy and Ni_3S_2 can also be confirmed by the work function calculation below.

Acidic and alkaline HER performance

A typical three-electrode system was used to evaluate the HER performance of Ni_3S_2/Pt_5Ru_1@NF in 1.0 M KOH and 0.1 M $HClO_4$ solutions. For comparison, we also synthesized control samples of Ni_3S_2/Pt@NF, Ni_3S_2/Ru@NF and commercial PtC@NF catalysts with similar noble metal loadings. The performance of the nickel foam substrate was also tested to prove that our catalytic activity mainly comes from the Ni_3S_2 and nanoalloys. The polarization curves of Ni_3S_2/Pt_5Ru_1@NF and the control samples are displayed in Fig. 2a, revealing that Ni_3S_2/Pt_5Ru_1@NF can reach a current density of 10 mA cm^{-2} with only a low overpotential of 13 mV in 1.0 M KOH, exceeding most Ni_3S_2-based catalysts.[15,26,27] Fig. 2b compares the overpotential values of Ni_3S_2/Pt_5Ru_1@NF and the control group at current densities of 10, 100 and 500 mA cm^{-2}. The results show that Ni_3S_2/Pt_5Ru_1@NF

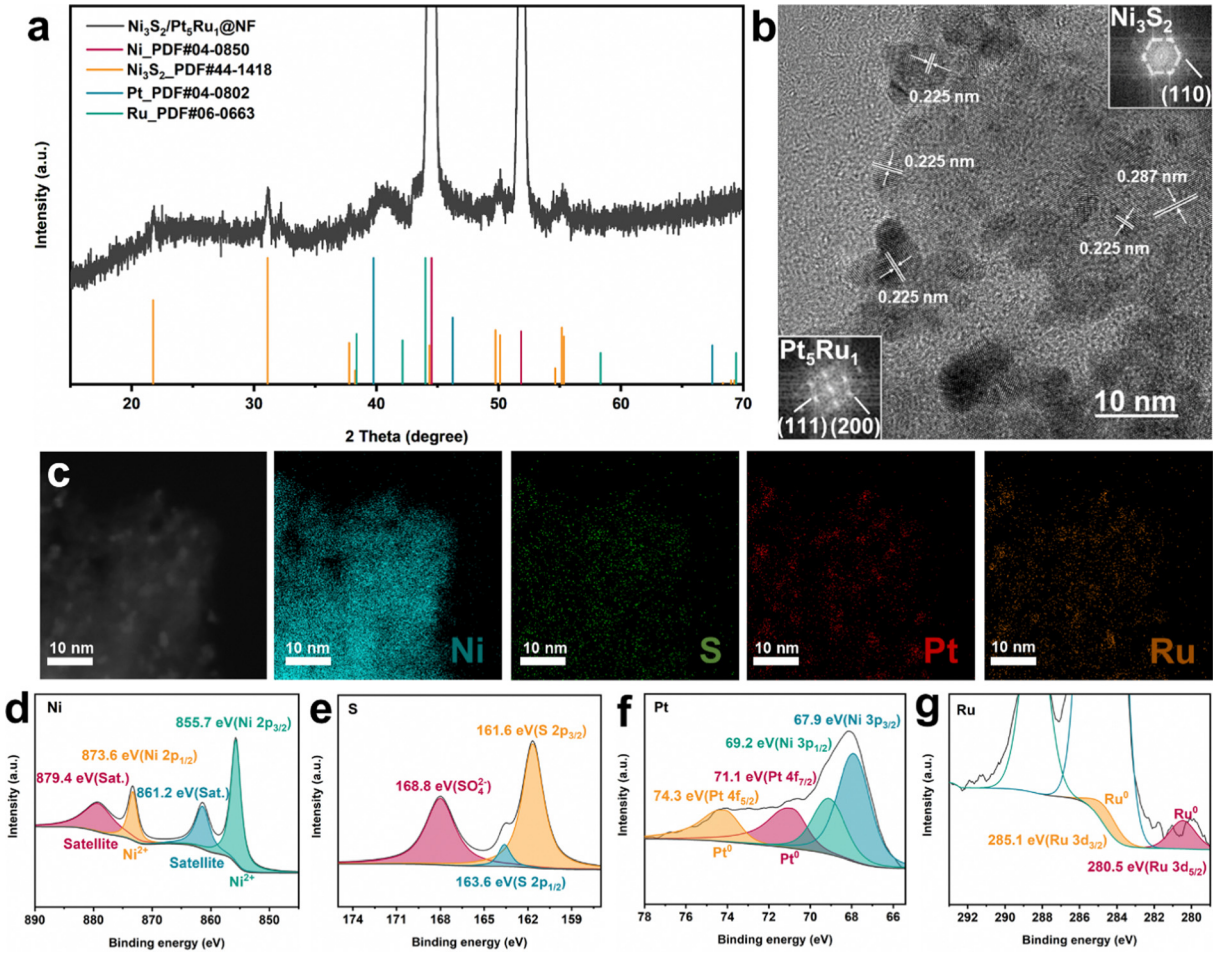

Fig. 1 Structural and microstructure characterizations of Ni_3S_2/Pt_5Ru_1@NF. (a) XRD pattern, (b) HRTEM image and the corresponding FFT patterns, (c) STEM image and the corresponding EDX elemental mapping images, and XPS spectra of (d) Ni 2p, (e) S 2p, (f) Pt 4f, and (g) Ru 3d.

has the smallest overpotential values at different current densities, and the performance is still better than that of commercial Pt/C. Electrochemically active surface area (ECSA) is often used to evaluate the actual catalytic performance of electrode materials. Since there is a linear relationship between ECSA and electric double-layer capacitance (C_{dl}), we utilized cyclic voltammetry (CV) to measure the C_{dl} of the catalyst at different scan rates, as shown in Fig. 2c. It can be observed that Ni_3S_2/Pt_5Ru_1@NF (22.7 mF cm^{-2}) has a C_{dl} close to that of Pt/C (26.9 mF cm^{-2}), and significantly higher than other control samples. The polarization curves of Ni_3S_2/Pt_5Ru_1@NF and control samples based on ECSA-normalization toward the HER in 1.0 M KOH are displayed in Fig. S5b (ESI†). The results show that Ni_3S_2/Pt_5Ru_1@NF also has the smallest overpotential values at different current densities. Fig. 2d tests the Tafel slopes of Ni_3S_2/Pt_5Ru_1@NF and the control samples. It is found that Ni_3S_2/Pt_5Ru_1@NF has a smaller Tafel slope, indicating a faster kinetic process at low potentials. The electrochemical impedance spectroscopy (EIS) of Ni_3S_2/Pt_5Ru_1@NF and the control samples was performed and simulated by a double-parallel equivalent circuit model (Fig. 2e and Table S2, ESI†). The first parallel component (T and R_1) reflects the charge transfer kinetics, where T is related to the electric double layer capacitance and R_1 represents the catalytic charge transfer resistance. Ni_3S_2/Pt_5Ru_1@NF has the smallest resistance after fitting, indicating its faster charge transfer process. The second parallel component (C_ψ and R_2) reflects the hydrogen adsorption behavior on the catalyst surface, where C_ψ and R_2 represent the hydrogen adsorption pseudo-capacitance and resistance, respectively. It can be observed from the fitting results in Table S2 (ESI†) that Ni_3S_2/Pt_5Ru_1@NF has a larger C_ψ and a smaller R_2, indicating that its unique 'metal–support' structure is more conducive to the binding of protons and the desorption of hydrogen on the surface. We also tested the long-term stability by chronopotentiometry measurement (Fig. 2f). At a constant current of 10 mA cm^{-2}, there is basically no obvious attenuation of the overpotential after 40 h for the Ni_3S_2/Pt_5Ru_1@NF, which formed a clear contrast with the commercial Pt/C catalyst after 2 h.

Likewise, the HER performance of Ni_3S_2/Pt_5Ru_1@NF in 0.1 M $HClO_4$ was also investigated. From the polarization curves in Fig. 3a and the comparison of the overpotential at different current densities in Fig. 3b, Ni_3S_2/Pt_5Ru_1@NF has similar overpotential to commercial Pt/C at a current density of

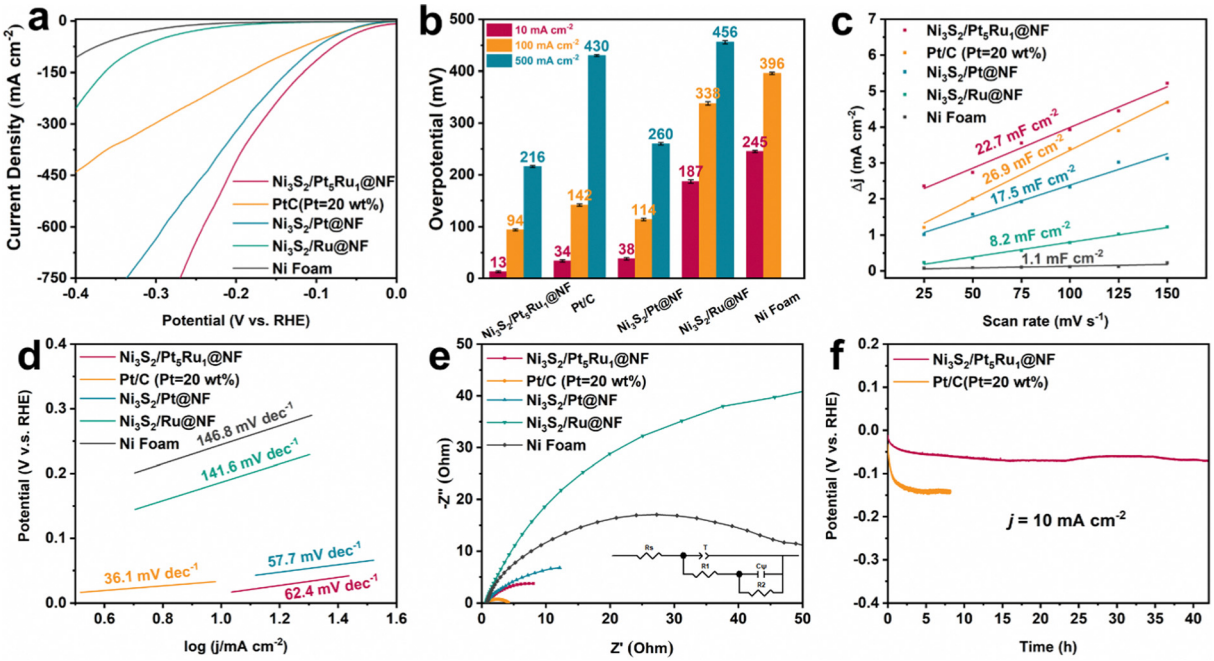

Fig. 2 Electrocatalytic HER performance in 1.0 M KOH solution. (a) Polarization curves of the electrocatalysts for the HER (with 95% iR compensation), (b) the resultant overpotentials at current densities of 10, 100 and 500 mA cm^{-2} for the as-prepared electrocatalysts, (c) calculated electrochemical double-layer capacitances, (d) the corresponding Tafel plots, (e) Nyquist plots under open-circuit voltage, and (f) long-term stability test at current densities of 10 mA cm^{-2}.

10 mA cm^{-2}. However, with the increase of the current density, the HER performance of Ni_3S_2/Pt_5Ru_1@NF gradually exceeds that of commercial Pt/C, and the overpotential of Ni_3S_2/Pt_5Ru_1@NF is even only half that of commercial Pt/C at a large current density of 100 mA cm^{-2}. This may be related to the extremely fast kinetic process of Ni_3S_2/Pt_5Ru_1@NF in acidic solution, which can also be demonstrated by the Tafel slope in Fig. 3c. Likewise, the polarization curves of Ni_3S_2/Pt_5Ru_1@NF

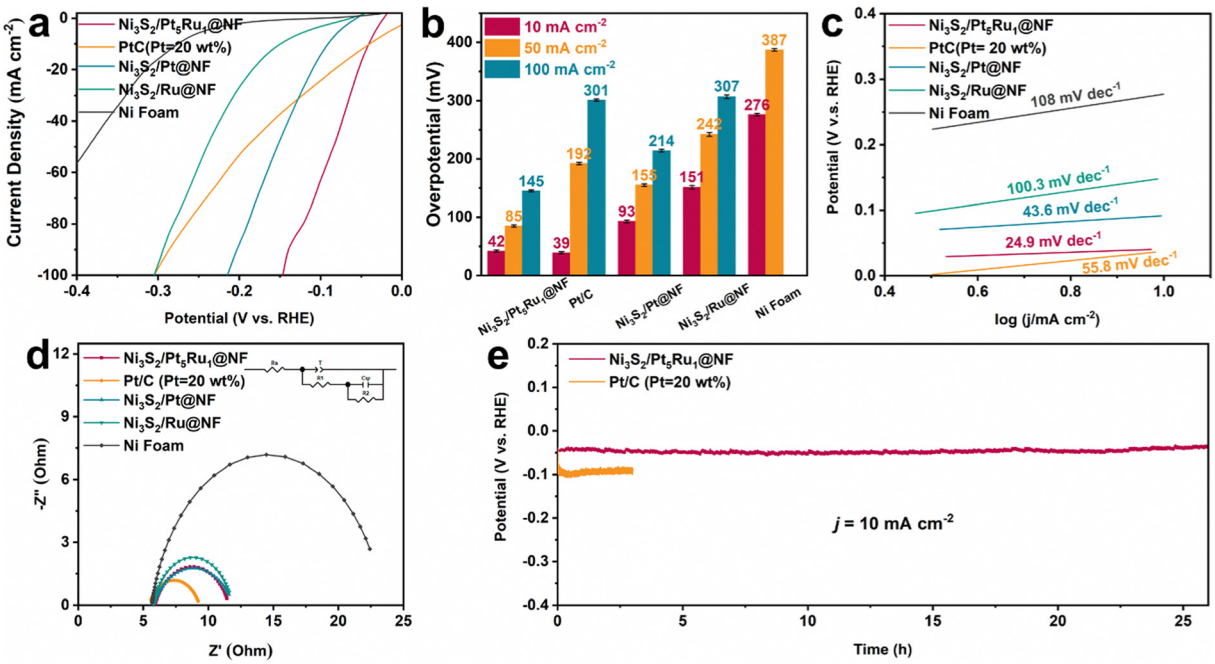

Fig. 3 Electrocatalytic HER performance in 0.1 M $HClO_4$ solution. (a) Polarization curves of the electrocatalysts for the HER (with 95% iR compensation), (b) the resultant overpotentials at current densities of 10, 50 and 100 mA cm^{-2} for the as-prepared electrocatalysts, (c) the corresponding Tafel plots, (d) Nyquist plots under open-circuit voltage, and (e) long-term stability test at current densities of 10 mA cm^{-2}.

and the control samples based on ECSA-normalization toward the HER in 0.1 M $HClO_4$ show a similar regularity (Fig. S5a, ESI†). The EIS of Ni_3S_2/Pt_5Ru_1@NF and control samples under acidic conditions were also fitted, as shown in Fig. 3d and Table S3 (ESI†). Like the results in 1.0 M KOH, the unique structural design of Ni_3S_2/Pt_5Ru_1@NF provides a good conductive network for the rapid transfer of protons and desorption of hydrogen. More excitingly, Ni_3S_2/Pt_5Ru_1@NF exhibits excellent durability in 0.1 M $HClO_4$ with almost no decay of the overpotential at a current density of 10 mA cm^{-2} (Fig. 3e), indicating that Ni_3S_2/Pt_5Ru_1@NF can exist stably for a long time in acidic solution. Compared with other nickel-based chalcogenide catalysts, the overpotential of Ni_3S_2/Pt_5Ru_1@NF is in a leading position, as shown in Table S4 (ESI†).

Experimental evidence for hydrogen spillover

The hydrogen spillover process is widespread on catalyst surfaces with at least two active sites, usually from sites with more negative ΔG_H to those with more positive ΔG_H. Generally, the HER involves a two-electron process, and the reaction pathway is as follows:

Acidic solution:

$$H^+ + e^- + * \rightarrow H^* \quad (1)$$

$$H^+ + e^- + H^* \rightarrow * + H_2\uparrow \quad (2)$$

Alkaline solution:

$$H_2O + e^- + * \rightarrow H^* + OH^- \quad (3)$$

$$H_2O + e^- + H^* \rightarrow * + OH^- + H_2 \quad (4)$$

In acidic solution, H^+ is preferentially adsorbed on the surface of the active site, taking electrons from the bulk to form protons. Proton and proton combine to form H_2 leaving the active site. For alkaline solutions, the first step is often the dissociation of H_2O in the active site. Herein, if it is necessary to prove the occurrence of the hydrogen spillover process, two points must be understood: (i) the intrinsic activity of the active site, and (ii) the change of the surface adsorption state. Therefore, we first tested the turnover frequency (TOF) of Ni_3S_2/Pt_5Ru_1@NF.[28] It can be seen from Fig. 4a that Ni_3S_2/Pt_5Ru_1@NF has the highest TOF value compared to the control samples, indicating that the active sites of Ni_3S_2/Pt_5Ru_1@NF have high intrinsic activity. The kinetic isotope effect (KIE) is normally used to estimate the involvement of proton transfer in the rate-determining step of an electrocatalytic reaction.[29] As shown in Fig. 4b, the KIE value of Ni_3S_2/Pt_5Ru_1@NF is over 1, implying that protons are involved in the HER reaction.[30] Compared with control samples, Ni_3S_2/Pt_5Ru_1@NF has the smallest KIE value, which indicates that Ni_3S_2/Pt_5Ru_1@NF has an extremely fast proton transfer kinetic process.[31] In order to further confirm the active sites of Ni_3S_2/Pt_5Ru_1@NF for the HER, poisoning tests were performed by adding thiocyanate (SCN^-) and tetramethylammonium cation (TMA^+) ions into acidic and alkaline solutions.[32] It has been reported that TMA^+ has adsorption properties for O-group elements.[33] In Ni_3S_2/Pt_5Ru_1@NF, it can be adsorbed on the S site to block the path of hydrogen

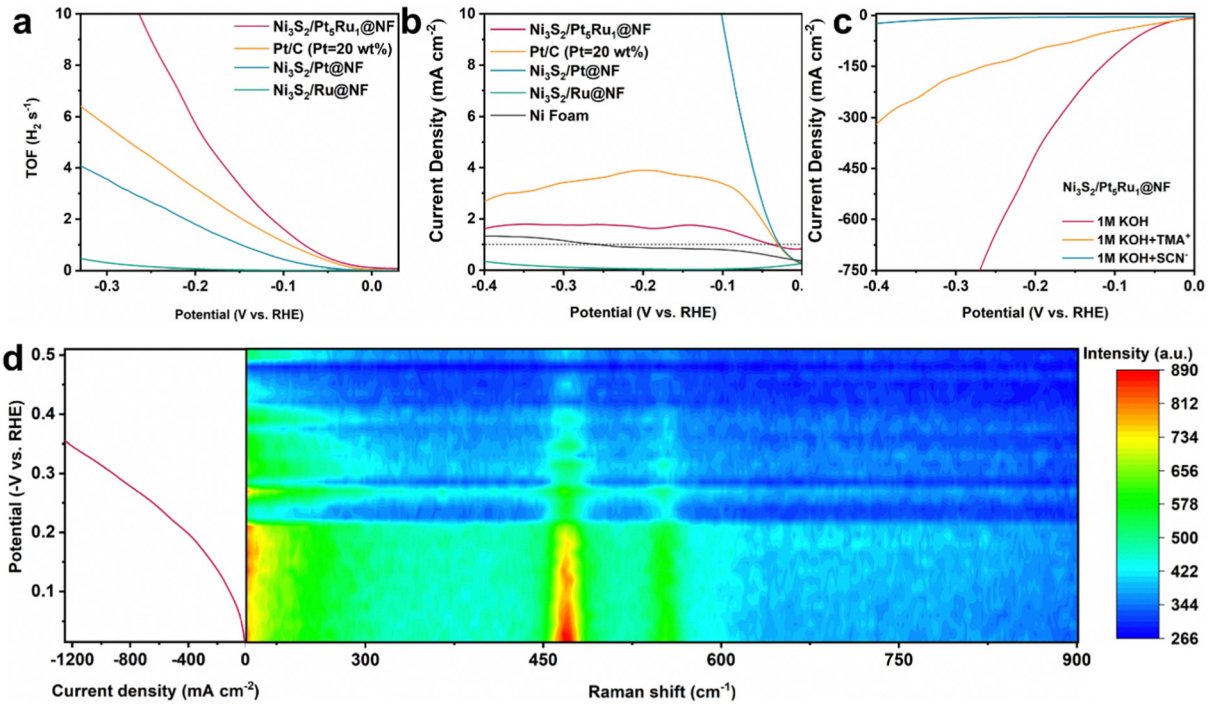

Fig. 4 Mechanism study of Ni_3S_2/Pt_5Ru_1@NF. (a) The potential-dependent TOF curves for Ni_3S_2/Pt_5Ru_1@NF, Pt/C, Ni_3S_2/Pt@NF and Ni_3S_2/Ru@NF, (b) calculated KIE values (JH_2O/JD_2O) from Ni_3S_2/Pt_5Ru_1@NF, Pt/C, Ni_3S_2/Pt@NF, Ni_3S_2/Ru@NF and Ni foam, (c) polarization curves for Ni_3S_2/Pt_5Ru_1@NF before and after the addition of SCN^- and TMA^+ ions in N_2-saturated 1.0 M KOH, and (d) *operando* Raman spectra of Ni_3S_2/Pt_5Ru_1@NF in 1.0 M KOH under HER potential.

overflow. As a commonly used ion in poisoning experiments, SCN^- can be adsorbed on the surface of the Pt_5Ru_1 alloy to inactivate it. As shown in Fig. 4c, the addition of SCN^- and TMA^+ affects the HER response to varying degrees. TMA^+ blocks the path for hydrogen spillover, making the transfer of protons between active sites difficult, and SCN^- adsorption on the surface of Pt_5Ru_1 alloy poisons the catalyst, dropping the activity of Ni_3S_2/Pt_5Ru_1@NF almost to zero. The above results indicate that both Ni_3S_2 and Pt_5Ru_1 are involved in the HER as active sites. By the extent of the decrease in activity in Fig. 4c, we predict that Pt_5Ru_1 preferentially undergoes the Volmer step to generate protons due to its higher activity.

Although the above electrochemical methods can reveal the existence of active sites and the strength of activity in Ni_3S_2/Pt_5Ru_1@NF, the real hydrogen spillover process is hard to identify. The hydrogen spillover process itself is dynamic, and transient imaging technology with ultra-high spatial resolution and nanometer size should be used to monitor the hydrogen spillover process in real time.[34] Unfortunately, there is no available technology to visually observe the hydrogen spillover process. Considering that the catalytic reaction generally occurs at the surface interface, a surface-sensitive technique can be used to infer the occurrence of the hydrogen spillover process. Herein, we attempt to instantaneously record the HER of Ni_3S_2/Pt_5Ru_1@NF by operando Raman spectroscopy, and speculate the hydrogen spillover process *via* bonding changes on its surface.[35,36] The Raman spectra of Ni_3S_2/Pt_5Ru_1@NF and control samples were thus studied to obtain the information of surface bonding. As shown in Fig. S6a (ESI†), Raman signals appeared at 192, 224, 305, 326 and 353 cm^{-1} for Ni_3S_2/Pt_5Ru_1@NF and the control samples correspond to the E4, E3, E2, A1 and E1 vibrational states of Ni_3S_2, respectively, indicating that the Ni_3S_2 is abundant in the samples.[27] The signals of Pt and Ru are not detected, which may be related to the insensitivity of Raman spectroscopy

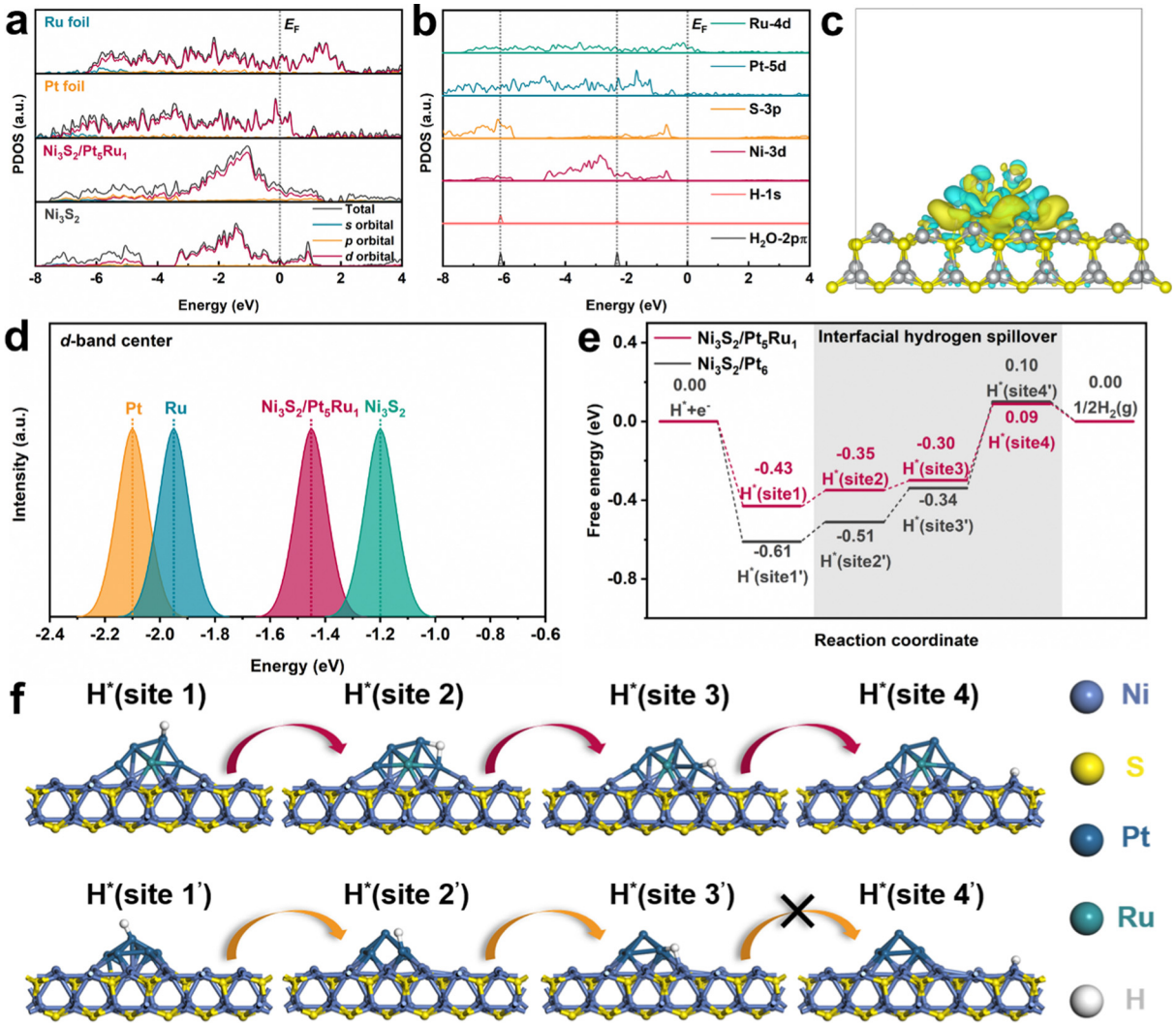

Fig. 5 DFT calculation, (a) calculated PDOS of Ni_3S_2/Pt_5Ru_1, Ni_3S_2, Ru foil and Pt foil with aligned Fermi level E_F, (b) the d–p orbital alignment of the surface Ru, Pt, S and Ni sites for Ni_3S_2/Pt_5Ru_1, (c) the local electron density distribution of the Pt_5Ru_1 cluster in Ni_3S_2/Pt_5Ru_1, (d) calculated d-band center (E_d) of Ni_3S_2/Pt_5Ru_1, Ni_3S_2, Ru foil and Pt foil, (e) calculated free energy diagram for the HER on Ni_3S_2/Pt_5Ru_1 paradigm and Ni_3S_2/Pt_6 benchmark, and (f) the optimized H* adsorption structures at various sites.

to metal elements. Fig. S6b (ESI†) compares the signals of 1.0 M KOH and Ni_3S_2/Pt_5Ru_1@NF in 1.0 M KOH, indicating that the new peaks appearing in Ni_3S_2/Pt_5Ru_1@NF are not the signals of KOH. Fig. S6c (ESI†) compares the spectral information of Ni_3S_2/Pt_5Ru_1@NF before and after adding 1.0 M KOH. After adding 1.0 M KOH, three new peaks appeared at 468, 549 and 1059 cm^{-1} correspond to Ni–O and two Ni–S bonds, respectively. A broad peak appears at 1635 cm^{-1}, associated with the H–OH bending vibration of adsorbed water. The above results indicate that after the addition of 1.0 M KOH, OH^- and H_2O in the solution will be adsorbed on the surface of Ni sites. Therefore, the hydrogen spillover process can be indirectly observed by change of the Ni–O bond on the surface of the Ni site at 468 cm^{-1}. As shown in Fig. 4d, the peak intensity of the Ni–O bond gradually weakens as the potential increases. This is because with the increase of the potential, the hydrogen overflow process of Ni_3S_2/Pt_5Ru_1@NF is continuously enhanced, and more and more protons are generated on the surface of the Pt_5Ru_1 alloy and overflow to the Ni sites in the Ni_3S_2 to form H_2. The adsorption state on the Ni surface gradually changed from Ni–O bonds to the adsorption of protons at Ni sites. This result is quite consistent with the hydrogen spillover process from the Pt_5Ru_1 alloy to Ni_3S_2 as we conceived.

DFT calculations for hydrogen spillover

Density functional theory (DFT) calculations were further performed to gain insights into the hydrogen spillover process. Combining XRD and HRTEM results, we choose the (110) facet of Ni_3S_2 as the substrate, and Pt_5Ru_1 clusters on it as the nanoalloy.[37] Details of the simulation models and DFT calculations are illustrated in the ESI.† Fig. 5a calculates the DOS and PDOS of Ni_3S_2/Pt_5Ru_1, Ni_3S_2, Ru foil and Pt foil. The results show that Pt_5Ru_1 increases the occupied state of Ni_3S_2 near the Fermi level, which means that Ni_3S_2/Pt_5Ru_1@NF can more easily obtain electrons from the bulk for the HER.[38] Fig. 5b calculates the PDOS of Ni_3S_2/Pt_5Ru_1 from the angle of Pt, Ru, S and Ni elements. The 1s orbital of H and the 2pπ orbital of H_2O overlap well with Ni_3S_2/Pt_5Ru_1. This means that H_2O or protons can make good contact with various elements at the interface of Ni_3S_2/Pt_5Ru_1@NF and transfer electrons during the reaction, which also explains the lower charge transfer resistance of Ni_3S_2/Pt_5Ru_1@NF in Fig. 2e and 3d. To intuitively describe the interaction between Ni_3S_2 substrate and Pt_5Ru_1 nanoalloy, we calculated the charge density difference of Ni_3S_2/Pt_5Ru_1. As shown in Fig. 5c, the Pt_5Ru_1 nanoalloy and Ni_3S_2 surface have good electron transfer, which means that Pt_5Ru_1 can be stably supported on Ni_3S_2 without being detached from the surface.[26] The d-band centers of Ni_3S_2/Pt_5Ru_1, Ni_3S_2, Pt foil and Ru foil were calculated by DOS, as shown in Fig. 5d. The lower the d-band center, the lower the position of the antibonding orbital and the lower the adsorption energy. According to previous literature reports, Pt and Ru have the most excellent adsorption energy, allowing protons to react and forming H_2 off the surface.[39,40] Compared with Ni_3S_2, Ni_3S_2/Pt_5Ru_1 has a d-band center closer to Pt and Ru, so protons are more likely to be adsorbed and desorbed on the surface of Ni_3S_2/Pt_5Ru_1. The above calculations indicate that Ni_3S_2/Pt_5Ru_1@NF itself has good electrical conductivity and moderate hydrogen adsorption energy, and is an excellent catalyst for the HER.

The above evidence, however, is not enough to prove that Ni_3S_2/Pt_5Ru_1@NF can generate hydrogen spillover. In theory, two conditions are required to produce hydrogen spillover: (i) There is a difference in the free energy of hydrogen evolution (G_H) between the active sites. The ions preferentially undergo the Volmer step to form protons at the more negative ΔG_H sites, and the protons then transfer to the more positive ΔG_H sites to undergo the Tafel step to form the H_2. (ii) The transfer between active sites should have a smaller migration energy barrier to reduce obstruction of hydrogen spillover. For the convenience of comparison, we chose Ni_3S_2/Pt_6 as the control sample, and took the HER reaction mechanism under acidic conditions as the overall design framework. The ΔG_H of Ni_3S_2/Pt_5Ru_1 and Ni_3S_2/Pt_6 was calculated in an attempt to construct a hydrogen spillover path. As shown in Fig. 5e and f, the optimized hydrogen spillover path reveals that the uniquely 'metal–support' structured Ni_3S_2/Pt_5Ru_1 has a suitable ΔG_H compared with Ni_3S_2/Pt_6. H^+ preferentially adsorbs to site 1 of the Pt_5Ru_1 alloy with a ΔG_H of −0.43 eV, and gains electrons from the Pt_5Ru_1 alloy site to form protons. It is then transferred to the interface of the alloy and substrate through site 2 and site 3 of Pt_5Ru_1, and finally H_2 leaves the surface with a ΔG_H of 0.09 eV at the Ni site of Ni_3S_2. On the other hand, it is well known that due to the difference in work function between the metal and the support, a Schottky barrier is inevitably formed, which traps protons at the interface and hinders hydrogen spillover. Therefore, reducing the work function difference ($\Delta\phi$) as much as possible is an effective method to enhance the hydrogen spillover process. Here, we calculated $\Delta\phi$ between Ni_3S_2 and Pt (Pt_5Ru_1). The calculated results are shown in Fig. S7 and S8 (ESI†). $\Delta\phi$ between Pt_5Ru_1 and Ni_3S_2 is 0.5678 eV, which is significantly smaller than 0.8442 eV between Pt and Ni_3S_2. That is to say, the Schottky barrier at the Ni_3S_2/Pt_5Ru_1 interface is smaller, and protons are not easily captured at the interface, which is favorable for the occurrence of the hydrogen spillover process.

3. Conclusions

In summary, through a simple two-step synthesis, we designed a 'metal–support' structured Ni_3S_2/Pt_5Ru_1@NF catalyst with excellent catalytic performance under both acidic and basic conditions. Through the combination of experimental verification and theoretical calculation, the mechanism of the hydrogen spillover process is explained in detail. But as a new theory, the hydrogen spillover process itself needs more characterization methods to clarify its physical and chemical processes. As a successful case, Ni_3S_2/Pt_5Ru_1@NF provides strong proof for the development of this theory.

Author contributions

Y. Y. and X. R. conceived and supervised the research. Y. Y. and Z. Y. designed the experiments. Z. Y. performed the

experiments and data analysis. Z. Y. conducted DFT calculations. All the authors discussed the results and commented on the paper.

Conflicts of interest

There are no conflicts to declare.

Acknowledgements

This work was supported by the National Key R&D Program of China (Grant 2022YFA1504100), the National Natural Science Foundation of China (No. 51925207, U1910210 and 52161145101), the "Transformational Technologies for Clean Energy and Demonstration" Strategic Priority Research Program of Chinese Academy of Sciences (Grant No. XDA21000000), the National Synchrotron Radiation Laboratory (KY2060000173), the Fundamental Research Funds for the Central Universities (Wk2060140026), the Joint Fund of the Yulin University and the Dalian National Laboratory for Clean Energy (Grant No. YLU-DNL Fund 2021002).

Notes and references

1 P. De Luna, C. Hahn, D. Higgins, S. A. Jaffer, T. F. Jaramillo and E. H. Sargent, *Science*, 2019, **364**, eaav3506.
2 J. A. Turner, *Science*, 2004, **305**, 972–974.
3 S. Chu and A. Majumdar, *Nature*, 2012, **488**, 294–303.
4 J. K. Norskov, T. Bligaard, J. Rossmeisl and C. H. Christensen, *Nat. Chem.*, 2009, **1**, 37–46.
5 S. Hammes-Schiffer and G. Galli, *Nat. Energy*, 2021, **6**, 700–705.
6 S. L. Hu and W. X. Li, *Science*, 2021, **374**, 1360.
7 Z. W. Seh, J. Kibsgaard, C. F. Dickens, I. Chorkendorff, J. K. Norskov and T. F. Jaramillo, *Science*, 2017, **355**, eaad4998.
8 M. F. Li, K. N. Duanmu, C. Z. Wan, T. Cheng, L. Zhang, S. Dai, W. X. Chen, Z. P. Zhao, P. Li, H. L. Fei, Y. M. Zhu, R. Yu, J. Luo, K. T. Zang, Z. Y. Lin, M. N. Ding, J. Huang, H. T. Sun, J. H. Guo, X. Q. Pan, W. A. Goddard, P. Sautet, Y. Huang and X. F. Duan, *Nat. Catal.*, 2019, **2**, 495–503.
9 X. S. Wang, Y. Zheng, W. C. Sheng, Z. C. J. Xu, M. Jaroniec and S. Z. Qiao, *Mater. Today*, 2020, **36**, 125–138.
10 B. Zhao, D. Y. Shen, Z. C. Zhang, P. Lu, M. Hossain, J. Li, B. Li and X. D. Duan, *Adv. Funct. Mater.*, 2021, **31**, 2105132.
11 Z. P. Lin, B. B. Xiao, Z. P. Wang, W. Y. Tao, S. J. Shen, L. A. Huang, J. T. Zhang, F. Q. Meng, Q. H. Zhang, L. Gu and W. W. Zhong, *Adv. Funct. Mater.*, 2021, **31**, 2102321.
12 S. Jeong, H. D. Mai, T. K. Nguyen, J. S. Youn, K. H. Nam, C. M. Park and K. J. Jeon, *Appl. Catal., B*, 2021, **293**, 120227.
13 D. Reynard, B. Nagar and H. Girault, *ACS Catal.*, 2021, **11**, 5865–5872.
14 B. Geng, F. Yan, X. Zhang, Y. He, C. Zhu, S. L. Chou, X. Zhang and Y. Chen, *Adv. Mater.*, 2021, **33**, e2106781.
15 K. L. Zhou, C. B. Han, Z. Wang, X. Ke, C. Wang, Y. Jin, Q. Zhang, J. Liu, H. Wang and H. Yan, *Adv. Sci.*, 2021, **8**, 2100347.
16 Z. Wang, M. T. Tang, A. Cao, K. Chan and J. K. Nørskov, *J. Phys. Chem. C*, 2022, **126**, 5151–5158.
17 R. Prins, *Chem. Rev.*, 2012, **112**, 2714–2738.
18 W. Karim, C. Spreafico, A. Kleibert, J. Gobrecht, J. VandeVondele, Y. Ekinci and J. A. van Bokhoven, *Nature*, 2017, **541**, 68–71.
19 J. Li, J. Hu, M. Zhang, W. Gou, S. Zhang, Z. Chen, Y. Qu and Y. Ma, *Nat. Commun.*, 2021, **12**, 3502.
20 Z. W. Wei, H. J. Wang, C. Zhang, K. Xu, X. L. Lu and T. B. Lu, *Angew. Chem., Int. Ed.*, 2021, **60**, 16622–16627.
21 G. Ren, Q. Hao, J. Mao, L. Liang, H. Liu, C. Liu and J. Zhang, *Nanoscale*, 2018, **10**, 17347–17353.
22 H. Du, R. Kong, F. Qu and L. Lu, *Chem. Commun.*, 2018, **54**, 10100–10103.
23 N. Chen, Y. X. Du, G. Zhang, W. T. Lu and F. F. Cao, *Nano Energy*, 2021, **81**, 105605.
24 T. Wang, X. Cao and L. Jiao, *eScience*, 2021, **1**, 69–74.
25 X. W. Lv, P. Kannan, S. Ji, X. Y. Wang and H. Wang, *CrystEngComm*, 2020, **22**, 6517–6528.
26 B. Fei, Z. L. Chen, J. X. Liu, H. B. Xu, X. X. Yan, H. L. Qing, M. Chen and R. B. Wu, *Adv. Energy Mater.*, 2020, **10**, 2001963.
27 S. C. Huang, Y. Y. Meng, Y. F. Cao, F. Yao, Z. J. He, X. X. Wang, H. Pan and M. M. Wu, *Appl. Catal., B*, 2020, **274**, 119120.
28 X. Li, Y. Fang, J. Wang, H. Fang, S. Xi, X. Zhao, D. Xu, H. Xu, W. Yu, X. Hai, C. Chen, C. Yao, H. B. Tao, A. G. R. Howe, S. J. Pennycook, B. Liu, J. Lu and C. Su, *Nat. Commun.*, 2021, **12**, 2351.
29 C. Pasquini, I. Zaharieva, D. Gonzalez-Flores, P. Chernev, M. R. Mohammadi, L. Guidoni, R. D. L. Smith and H. Dau, *J. Am. Chem. Soc.*, 2019, **141**, 2938–2948.
30 Y. Kong, Y. Li, X. Sang, B. Yang, Z. Li, S. Zheng, Q. Zhang, S. Yao, X. Yang, L. Lei, S. Zhou, G. Wu and Y. Hou, *Adv. Mater.*, 2022, **34**, e2103548.
31 X. Wang, X. Sang, C. L. Dong, S. Yao, L. Shuai, J. Lu, B. Yang, Z. Li, L. Lei, M. Qiu, L. Dai and Y. Hou, *Angew. Chem., Int. Ed.*, 2021, **60**, 11959–11965.
32 B. Q. Li, C. X. Zhao, J. N. Liu and Q. Zhang, *Adv. Mater.*, 2019, **31**, e1808173.
33 Z. F. Huang, J. J. Song, Y. H. Du, S. B. Xi, S. Dou, J. M. V. Nsanzimana, C. Wang, Z. C. J. Xu and X. Wang, *Nat. Energy*, 2019, **4**, 329–338.
34 T. Kosmala, A. Baby, M. Lunardon, D. Perilli, H. Liu, C. Durante, C. Di Valentin, S. Agnoli and G. Granozzi, *Nat. Catal.*, 2021, **4**, 850–859.
35 J. K. Li and J. L. Gong, *Energy Environ. Sci.*, 2020, **13**, 3748–3779.
36 X. Liu, J. Meng, J. Zhu, M. Huang, B. Wen, R. Guo and L. Mai, *Adv. Mater.*, 2021, **33**, e2007344.
37 X. Guo, X. Wan, Q. Liu, Y. Li, W. Li and J. Shui, *eScience*, 2022, **2**, 304–310.
38 K. Xu, P. Chen, X. Li, Y. Tong, H. Ding, X. Wu, W. Chu, Z. Peng, C. Wu and Y. Xie, *J. Am. Chem. Soc.*, 2015, **137**, 4119–4125.

39 Y. Zhao, P. V. Kumar, X. Tan, X. Lu, X. Zhu, J. Jiang, J. Pan, S. Xi, H. Y. Yang, Z. Ma, T. Wan, D. Chu, W. Jiang, S. C. Smith, R. Amal, Z. Han and X. Lu, *Nat. Commun.*, 2022, **13**, 2430.

40 L. Han, H. Cheng, W. Liu, H. Li, P. Ou, R. Lin, H. T. Wang, C. W. Pao, A. R. Head, C. H. Wang, X. Tong, C. J. Sun, W. F. Pong, J. Luo, J. C. Zheng and H. L. Xin, *Nat. Mater.*, 2022, **21**, 681–688.